AGU PUBLICATIONS

JGR

Journal of Geophysical Research: Planets

RESEARCH ARTICLE
10.1002/2016JE005038

Key Points:
- Target conditions found to have an important effect on basin subsurface morphology
- Revised current impact scaling relationships applicable to the lunar setting
- Estimates of impact conditions and transient crater diameters for impact basins mapped by GRAIL

Supporting Information:
- Supporting Information S1

Correspondence to:
K. Miljković,
katarina.miljkovic@curtin.edu.au

Citation:
Miljković, K., G. S. Collins, M. A. Wieczorek, B. C. Johnson, J. M. Soderblom, G. A. Neumann, and M. T. Zuber (2016), Subsurface morphology and scaling of lunar impact basins, *J. Geophys. Res. Planets*, *121*, 1695–1712, doi:10.1002/2016JE005038.

Received 23 MAR 2016
Accepted 17 AUG 2016
Accepted article online 20 AUG 2016
Published online 17 SEP 2016

Subsurface morphology and scaling of lunar impact basins

K. Miljković[1,2], G. S. Collins[3], M. A. Wieczorek[4], B. C. Johnson[1,5], J. M. Soderblom[1], G. A. Neumann[6], and M. T. Zuber[1]

[1]Department of Earth, Atmospheric, and Planetary Sciences, Massachusetts Institute of Technology, Cambridge, Massachusetts, USA, [2]Department of Applied Geology, Curtin University, Perth, Western Australia, Australia, [3]Department of Earth Sciences and Engineering, Imperial College London, London, UK, [4]Institut de Physique du Globe de Paris, Sorbonne Paris Cité, Université Paris Diderot, Paris, France, [5]Now at Department of Earth, Environmental, and Planetary Sciences, Brown University, Providence, Rhode Island, USA, [6]Solar System Exploration Division, NASA Goddard Space Flight Center, Greenbelt, Maryland, USA

Abstract Impact bombardment during the first billion years after the formation of the Moon produced at least several tens of basins. The Gravity Recovery and Interior Laboratory (GRAIL) mission mapped the gravity field of these impact structures at significantly higher spatial resolution than previous missions, allowing for detailed subsurface and morphological analyses to be made across the entire globe. GRAIL-derived crustal thickness maps were used to define the regions of crustal thinning observed in centers of lunar impact basins, which represents a less unambiguous measure of a basin size than those based on topographic features. The formation of lunar impact basins was modeled numerically by using the iSALE-2D hydrocode, with a large range of impact and target conditions typical for the first billion years of lunar evolution. In the investigated range of impactor and target conditions, the target temperature had the dominant effect on the basin subsurface morphology. Model results were also used to update current impact scaling relationships applicable to the lunar setting (based on assumed target temperature). Our new temperature-dependent impact-scaling relationships provide estimates of impact conditions and transient crater diameters for the majority of impact basins mapped by GRAIL. As the formation of lunar impact basins is associated with the first ~700 Myr of the solar system evolution when the impact flux was considerably larger than the present day, our revised impact scaling relationships can aid further analyses and understanding of the extent of impact bombardment on the Moon and terrestrial planets in the early solar system.

1. Introduction

Impact processes played an important role in the evolution of the early solar system. During this time, the impact bombardment rate may have been greater by several orders of magnitude in comparison to the impact flux of today. As a result, planetary bodies in the inner solar system would have been heavily battered, and their surfaces sculpted, by large impacts. This epoch of high impact fluxes could have lasted hundreds of millions of years [*Tera et al*., 1974; *Kring and Cohen*, 2002; *Gomes et al*., 2005], with a gradually declining impact flux [*Bottke et al*., 2012; *Johnson and Melosh*, 2012].

All lunar impact basins (craters larger than ~200 km in rim-to-rim diameter) formed between the period of ~4.5 billion years ago (Gya) when the Moon formed and no later than 3.73 Gya when Orientale, the last large basin, formed [*Stöffler and Ryder*, 2001; *Le Feuvre and Wieczorek*, 2011]. A few tens of large impact basins were observed [e.g., *Wilhelms*, 1987; *Fassett et al*., 2012; *Neumann et al*., 2015], which have been categorized by size and surface morphology. In general, a morphological continuum has been identified between protobasins (the smallest basins) and peak-ring to multiring (the largest) basins [e.g., *Hartmann and Kuiper*, 1962; *Melosh*, 1989; *Spudis*, 1993; *Baker et al*., 2011; *Osinski and Pierazzo*, 2012]. However, given that some basins have multiple rings, and that portions of their defining morphological characteristics may no longer be observable, it has not always been possible to obtain a well-defined size for many of these basins.

The deep structure of lunar impact basins has been investigated previously by the inversion of gravity data obtained by Apollo spacecraft [e.g., *Müller and Sjogren*, 1968; *Wise and Yates*, 1970; *Phillips et al*., 1972; *Bratt et al*., 1985]. It was suggested that the crust in the central areas of several large lunar basins (on the nearside hemisphere) is thinned with respect to the ambient crustal thickness and that the crust-mantle interface

beneath these basins was elevated, implying that mantle material was uplifted toward the surface. An analysis of Clementine gravity and topography data provided further confirmation that lunar basins are characterized by a centrally uplifted crust-mantle interface that is surrounded by rings of thickened crust lying mainly within the main basin rim [e.g., *Zuber et al*., 1994; *Neumann et al*., 1996; *Wieczorek and Phillips*, 1999]. Numerical impact studies [*Ivanov et al*., 2010; *Potter et al*., 2012a, 2012b; *Melosh et al*., 2013; *Miljković et al*., 2013, 2015; *Freed et al*., 2014; *Potter et al*., 2015] have reinforced the idea that the basin-forming process excavates and displaces material in the central region of the crater, forming a central zone of thinned crust and uplifting underlying mantle material. Using this region of crustal thinning as a measure of basin size offers advantages over measurements of basin ring diameters derived from topography and imaging data, because basins often possess two or more rings, and the assignment of a specific ring as a crater diameter has been fraught with controversy. Even though basin rings might be degraded by erosion and/or buried by subsequent cratering, the subsurface morphology as determined by gravity measurements is preserved.

Gravity measurements of the Moon obtained by the Gravity Recovery and Interior Laboratory (GRAIL) mission [*Zuber et al*., 2013] provided the highest spatial resolution with global coverage to date. Recent GRGM900C model, based on data acquired during the GRAIL extended mission, is expanded to spherical harmonic degree 900, which corresponds to a half-wavelength spatial resolution of about 6 km [*Lemoine et al*., 2014]. This unprecedented data resolution has enabled a detailed analysis of subsurface structure in lunar impact basins across the entire globe for the first time. In this study, we used maps of the lunar crustal thickness derived from the GRAIL gravity data [*Wieczorek et al*., 2013] and topography obtained by the Lunar Orbiter Laser Altimeter (LOLA) on board the Lunar Reconnaissance Orbiter [*Smith et al*., 2010] to define diameters of the crustal thinning regions (D_{thin}) for a majority of recognized lunar impact basins [*Neumann et al*., 2015].

Basin-forming impacts on the Moon were modeled numerically by using the iSALE-2D hydrocode, and the simulation results were compared with inferred subsurface morphology of lunar basins. Using the simulation results, we revised crater-size scaling relationships applicable to basins that formed on the Moon. We also quantified the sensitivity of the transient crater size and the crust-mantle interface structure to plausible variations in target properties across the Moon (namely, temperature and crustal thickness). Using the revised crater scaling relationships, estimates of impact conditions that formed lunar impact basins, depending on the regional location of the basins, can be made.

2. Numerical Impact Methodology

We used the iSALE hydrocode to simulate the formation of lunar impact basins for a range of target properties typical for the Moon at the time of lunar basins formation. We consider (a) customized temperature-depth profiles obtained from lunar thermal evolution models [*Laneuville et al*., 2013] and (b) a range of ambient crustal thicknesses typical for the Moon as indicated by GRAIL observations [*Wieczorek et al*., 2013]. The employed methodology was the same as described by *Miljković et al*. [2013, 2015], which is similar to previous models by *Ivanov et al*. [2010], *Potter et al*. [2012a, 2012b, 2015], *Melosh et al*. [2013], and *Freed et al*. [2014].

2.1. Numerical Setup of iSALE-2D Hydrocode

iSALE is a multimaterial, multirheology finite difference shock-physics code used for simulating impact processes in geologic media [*Amsden et al*., 1980; *Collins et al*., 2004; *Wünnemann et al*., 2006]. It uses an equation of state and a constitutive model to describe material response to shock and the ensuing crater formation. The equation of state relates changes in material density and internal energy to pressure (the isotropic part of the full stress tensor), and the constitutive model relates changes in material distortion (shape) to the deviatoric part of the stress tensor. The iSALE code has been benchmarked against other hydrocodes used for modeling impact processes [*Pierazzo et al*., 2008].

All impact simulations assumed a vertical impact orientation enforced by the cylindrical symmetry of the model. The Eulerian mesh was composed of cells that were 1.5×1.5 km in size in simulations where the projectile diameter ranged from 30 to 90 km, and 0.5×0.5 km in size in simulations where the projectile was 15 km in diameter, implying a minimum resolution of 15 cells per projectile radius. Above this minimum resolution, the choice of the cell size did not affect the results, producing similar crust-mantle profiles and, most importantly, the same crustal thinning diameters.

In the majority of simulations an impact speed of 17 km s^{-1} was used. An impact speed of 10 km s^{-1} was used in some cases to observe the change in basin morphology produced by different impact speeds within the expected impact speed range during the epoch of basin formation [*Le Feuvre and Wieczorek*, 2011; *Bottke et al*., 2012]. Although these speeds represent the vertical impact velocity, they can also be regarded as a proxy for faster, moderately oblique incidence angles (>40°), because final basin diameter scales with the vertical component of an oblique velocity vector [*Pierazzo and Melosh*, 2000]. In other words, vertical impact simulations at a speed of 10 km s^{-1} are a reasonable proxy for impacts of the same size impactor at speeds of 14 and 11.5 km s^{-1} for impact trajectories at angles of 45° and 60° measured from the horizontal, respectively. This assumption does not extend to all aspects of the cratering process (for example, the expulsion of high-speed ejecta from the crater is very sensitive to impact speed and angle variations) but is presumed to be valid for the interior crater structure that is largely axially symmetric because of the nature of propagation of the impact-generated shock wave through the target [*Melosh*, 1989]. Numerical modeling studies [e.g., *Elbeshausen et al*., 2009] have shown that the morphology of large impact craters is axially symmetric for impacts at angles larger than 30° and reinforce the notion that crater size scales with the vertical component of the impact velocity.

The range of impactor size and velocity used in this study spans impacts that produce craters from small peak-ring basins to larger multiring basins on the Moon. All simulations assume a flat lunar surface. Lunar surface curvature does not play a significant role in defining the crustal thinning diameter, as the observed crustal thinning diameters are small compared to the radius of the Moon. However, we do not model the South Pole-Aitken (SP-A) basin, which is large enough to have had experienced the curvature effects during its formation.

The numerical mesh was divided into two horizontal layers representing the lunar crust and mantle, and the thickness of the preimpact crust was fixed at either 30, 45, or 60 km. The 30 km thick crust corresponds to the thinnest crust found on the nearside hemisphere (excluding the interior of large basins), and the 60 km thickness is representative of the farside hemisphere, as derived from the GRAIL crustal thickness model of *Wieczorek et al*. [2013]. Basalt and dunite have similar rheologic properties and densities to the lunar crust and mantle; therefore, those two materials were chosen to be representative of the crust and mantle layers, respectively. Dunite was also used to represent the projectile. In this work, we used the same material setup as detailed in *Miljković et al*. [2013, 2015].

Equation-of-state tables derived by using ANalytical Equation Of State with parameters for basalt [*Pierazzo et al*., 2005] and dunite [*Benz et al*., 1989] were combined with a strength and failure model described by *Collins et al*. [2004] for which the model parameters were defined by *Pierazzo et al*. [2005] (basalt) and *Ivanov et al*. [2010] (dunite). Additional simulations that used granite instead of basalt to represent the crust confirmed that the consequences of a basin forming event are insensitive to the chosen equation of state for the crustal material, provided that the bulk density is appropriate to represent the Moon's crust.

The initial analysis of the GRAIL gravity data revealed that the lunar crust has an average porosity of about 7–12% in the upper several kilometers, with significant porosity extending perhaps into even the upper mantle [*Wieczorek et al*., 2013]. Subsequent analyses have shown that the porosity profile can be approximated by an exponential function, possessing a surface value of about 24% and an *e*-folding depth scale of about 9 km [*Besserer et al*., 2014]. GRAIL-observed Bouguer anomalies of lunar complex craters suggested that the impact-generated porosity is limited to ~8 km depth, which could be associated with the thickness of the lunar megaregolith [*Soderblom et al*., 2015]. *Milbury et al*. [2015] showed that the porosity plays a dominant role in gravitational signature of small complex craters, whereas in larger craters mantle uplift was involved in the crater formation, so the gravitational Bouguer anomaly became dominantly positive and porosity was less important. All of our investigated and modeled lunar basins include prominent mantle uplifts. Therefore, we did not employ iSALE's porosity compaction model [*Wünnemann et al*., 2006] in our simulations for simplicity and because the basin formation process is driven by uplift of deep mantle rocks with little porosity.

2.2. Temperature Profiles Applied in Numerical Impact Simulations

Previous basin modeling studies emphasized the importance of preimpact target temperature on the basin formation process through its control on target strength [*Ivanov et al*., 2010; *Potter et al*., 2012a; *Miljković et al*., 2013; *Freed et al*., 2014; *Miljković et al*., 2015; *Potter et al*., 2015]. Following our previous work [*Miljković*

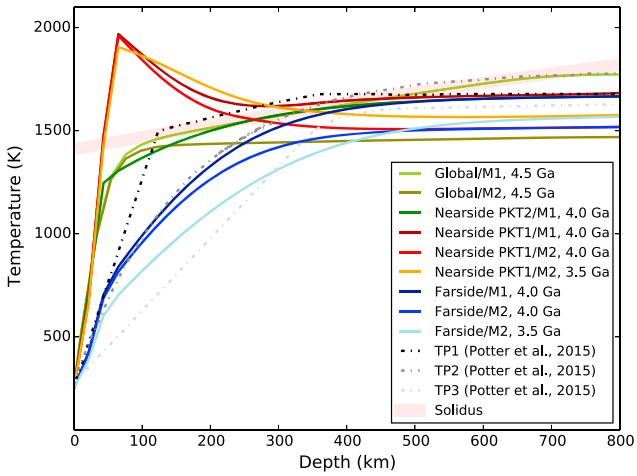

Figure 1. Temperature profiles used in iSALE-2D modeling of lunar impact basin formation. Global denotes the average temperature profile at 4.5 Ga ago following the magma ocean crystallization. "Nearside PKT1" and "Nearside PKT2" denote the different representations of the PKT region, and "Farside" denotes the farside hemisphere, all at later epochs (4.0 and 3.5 Ga). The designations M1 and M2 denote two different initial conditions for the mantle temperature profile. The temperature profiles were adopted from the 3D lunar thermal-evolution models of *Laneuville et al*. [2013]. The dashed lines (TP1, TP2, and TP3) show the temperature profiles used in similar work by *Potter et al*. [2015].

et al., 2013, 2015], we consider a large suite of representative temperature profiles obtained from the three-dimensional lunar thermal evolution models of *Laneuville et al*. [2013]. These models account for the asymmetric distribution of crustal heat production, and we utilized nine different temperature profiles in our iSALE-2D numerical impact simulations (Figure 1). Similar, but smaller, family of temperature profiles was used in *Miljković et al*. [2013, 2015].

Three different epochs in lunar evolution were investigated: 4.5 Ga (the epoch just after the formation of the Moon), 4.0 Ga, and 3.5 Ga, to account for different basin ages and/or possible variation in the temperature profiles during the basin-forming epoch. The temperature profiles for these three time periods are shown in Figure 1. In this figure, "Global" denotes the temperature profile at 4.5 Ga ago, which represents a 1-D profile representative of both hemispheres of the Moon just after magma ocean crystallization. "Nearside" and "Farside" represent the two hemispheres at two later epochs (4.0 and 3.5 Ga) that differ as a result of the enhanced heat production on the nearside of the Moon in the PKT [*Laneuville et al*., 2013]. The enrichment in heat-producing elements in the nearside hemisphere was represented by two different profiles: PKT1 and PKT2; PKT1 denotes enhanced heat production at the base of the nearside crust, whereas PKT2 denotes the same amount of enhanced heat production, but distributed uniformly within the nearside crust. Designations M1 and M2 denote two different initial conditions that were tested for the mantle temperature profile; M1 denotes an initial temperature profile that follows the solidus for the upper 350 km and an adiabatic gradient below, whereas M2 denotes an initial temperature profile that is set to an adiabat for the entire mantle. For comparison, Figure 1 also includes the temperature profiles used by *Potter et al*. [2015].

3. Numerical Modeling of Lunar Impact Basins

Numerical impact modeling of the lunar basin-forming process is used to (a) investigate the subsurface morphology of lunar basins and its dependence on a target temperature and crustal thickness and (b) improve impact-scaling relationships between impact and final basin morphology.

3.1. Subsurface Morphology of Impact Basins

Impact basins form via the growth of a bowl-shaped transient cavity. The excavated crust overturns on the outside of the transient crater as a thick ejecta deposit, and the transient crater undergoes complex collapse to produce the final basin morphology. The collapse of the transient crater involves a combination of inward motion of the cavity walls and prominent uplift of the cavity floor [e.g., *Melosh*, 1989]. The inward motion of the cavity walls includes a portion of the freshly overturned crustal material and can be sufficiently extreme that it sometimes covers up the uplifted material, forming a new "crustal cap" over the basin floor [*Freed et al*., 2014]. The uplift of the transient crater floor brings originally deep-seated lower crust and upper mantle toward (and, in some cases, onto) the surface, depending on target properties and impact conditions [*Miljković et al*., 2015]. The relative extent of wall collapse and floor uplift, as well as their interaction, depends on the shear strength and temperature of the crust and upper mantle as well as crater size [*Potter et al*., 2012a, 2015; *Miljković et al*., 2013, 2015].

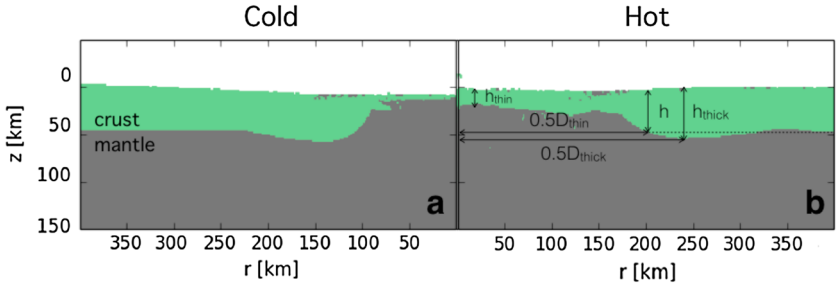

Figure 2. Crater measurements from iSALE-2D simulations, for an impact into (a) a cold target and (b) a hot target, demonstrating different morphological outcomes dependent on the target temperature. The final basin morphology showing the diameters of crustal thinning D_{thin} and crustal thickening D_{thick}. Parameter h is the preimpact crustal thickness, h_{thin} is the thickness of the crustal cap located in the basin center, and h_{thick} is the crustal thickness at D_{thick}. The crust is shown in green, and the mantle in grey.

During the early stages of the cratering process, the excavation flow opens an approximately hemispherical cavity that grows at a steadily decreasing rate until a maximum depth is reached [*Melosh*, 1989]. In small, simple craters, the transient crater refers to the form of a crater prior to collapse of the steep rim walls. The transient crater depth is the maximum depth of this cavity, and the transient crater diameter is the cavity diameter just prior to collapse. However, in the large crater (basin) formation regime, crater floor uplift can precede rim collapse by a considerable time interval. An unambiguous way to define the transient crater diameter in a basin-forming simulation is by using the width of the crater at the moment when the maximum crater volume is reached [*Elbeshausen et al*., 2009]. The transient crater diameter is always measured at the preimpact target level. It is reached a couple of minutes after initiation of the impact, and the final morphology is reached within 2 h. At this time, the final basin morphology means that the crater has finished forming; however, in most cases it is left with a central melt pool that cools over geologic time and the overall structure may continue to relax [e.g., *Freed et al*., 2014]. We consider these to be second-order effects on the shape of the crater and do not consider them further in this work.

The simulation depicted in Figure 2 illustrates the consequences of a vertical impact at 17 km/s by an impactor that is 45 km in diameter into a 45 km thick crust. Figures 2a and 2b show the final basin morphology for an impact into a cold and hot target, respectively; D_{thin} and D_{thick} are the diameters of the crustal thinning and crustal thickening regions, respectively; h_{thin} is the thicknesses of the crustal inflow (crustal cap) over the mantle uplift in the basin center; h_{thick} measures the crustal thickness at the crustal thickening region (the thickest crust within a basin); and h is the preimpact crustal thickness. D_{thin} was determined from the radius where the crustal thickness was first equal to the preimpact crustal thickness, and D_{thick} was determined from the radius from the basin center where crust was thickest. These parameters are measured in the same way in both the observed GRAIL-derived crustal thickness profiles and our iSALE impact simulations. Different outcomes shown in Figures 2a and 2b are showing morphological dependence on the target temperature alone.

The complete set of results from our iSALE-2D simulations is shown in Table S1 in the supporting information, including D_{tr}, D_{thin}, D_{thick}, h_{thin}, and h_{thick}, as labeled in Figure 2. A conservative uncertainty equivalent to two computational cells in length (cell length and width are equal) was associated with D_{thin}, D_{thick}, h_{thin}, and h_{thick}, because these parameters require defining the position of the surface and crust-mantle interface within mixed material cells. For impacts made by a 15 km projectile, the uncertainties ΔD_{thin}, ΔD_{thick}, Δh_{thin}, and Δh_{thick} were equal to 1 km; for larger projectiles, the uncertainties were 3 km.

3.2. Large Impact (Basin) Scaling Relationships

Traditionally, impact crater scaling equations provide a relationship between the size of a crater and its impact and target parameters. It is conventional to separate crater size scaling into two steps. One equation relates impactor and target parameters to the transient crater diameter (or volume). A second equation then accounts for the enlargement of the transient crater during crater collapse by relating transient and final crater diameter. The most widely used relationships describing the first step relate dimensionless measures of the impactor and transient crater size [e.g., *Holsapple and Schmidt*, 1987; *Holsapple*, 1993]. For craters larger

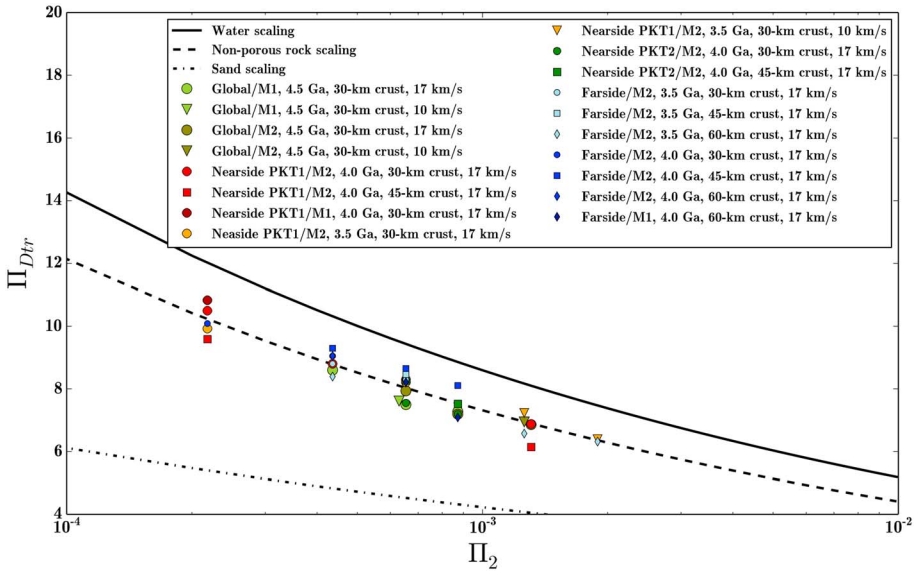

Figure 3. Numerical results from iSALE-2D hydrocode simulations made for nine different target temperature profiles and a combination of impact parameters (impact speeds at 10 or 17 km/s, and 30, 45, or 60 km preimpact crustal thickness). Our results satisfy the $\Pi_{D\mathrm{tr}}$-Π_2 impact-scaling law, for impacts into planar, homogenous, nonporous rock ($\Pi_{D\mathrm{tr}} = 1.60{\Pi_2}^{-0.22}$), assuming that the transient crater forms at the moment of the maximum cavity volume. Impact parameters included in this plot satisfy the most probable impact size and speed range for the formation of lunar impact basins (excluding the South Pole-Aitken basin).

than a few hundred meters on the Moon, the relevant measure of impactor size is the "gravity-scaled source size," $\Pi_2 = 1.6\, gL/\upsilon_2$, where L and υ are the impactor diameter and speed, respectively, and g is the gravitational acceleration. Transient crater diameter D_{tr} is nondimensionalized as $\Pi_D = D_{\mathrm{tr}}(\rho/M)^{1/3}$, where ρ is the density of the target and M is the mass of the impactor.

Normalized transient crater diameters obtained in previous numerical studies for a range of planetary-scale impacts appear to plot between the extrapolated trend lines for Ottawa sand ($\Pi_{D\mathrm{tr}} = 1.40{\Pi_2}^{-0.16}$) and water ($\Pi_{D\mathrm{tr}} = 1.88{\Pi_2}^{-0.22}$) [*Schmidt and Housen*, 1987; *Melosh*, 1989; *Ivanov et al*., 2010; *Potter et al*., 2012a, 2012b, 2013]. Figure 3 shows our numerical impact results for a number of combinations of impact parameters, chosen from among nine different temperature profiles, impact speeds of 10 or 17 km s^{-1} and 30, 45, or 60 km preimpact crustal thickness. The solid, dash-dotted, and dashed lines in Figure 3 show the best fit trendlines for impacts in water, sand, and competent (nonporous) rock, respectively [*Schmidt and Housen*, 1987; *Holsapple*, 1993]. All our simulations also satisfy the impact-scaling law for impacts into nonporous rock ($\Pi_{D\mathrm{tr}} = 1.60{\Pi_2}^{-0.22}$[*Melosh*, 1989]) and plot between the trend lines for sand and water.

If transient crater size could be determined from observations, it would provide an indirect method for estimating the impactor properties (or at least possible combinations of impactor size, speed, and density) using these transient-crater scaling laws. However, there is no evidence that transient craters can be confidently related to any topographic expressions associated with lunar impact basins. For example, recent detailed analyses of the youngest lunar impact basin, the Orientale basin, excluded any correlation between its transient crater diameter and diameters of any of its rings [*Johnson et al*., 2015].

An alternative scaling approach is to relate transient crater size to final crater structure by using numerical simulation results. We prefer to use the crustal thinning diameter (D_{thin}) as a new baseline for a basin's size because it can be readily observed in gravity data, it is better preserved than surface topography, and it can be easily measured in impact simulations. Figure 4 (top left) shows the relationship between the transient crater diameter and the final crustal thinning diameter (as denoted in Figure 2) measured from iSALE simulations for nine different temperature profiles associated with different locations and ages on the Moon. For similar temperature profiles, our numerical modeling results followed similar trends, and we grouped the temperature profiles accordingly: Nearside PKT1/M1 and Nearside PKT1/M2 at 4.0 and 3.5 Ga profiles were grouped under "hot" targets; PKT2/M2, Global/M1, and Global/M2 profiles were grouped under

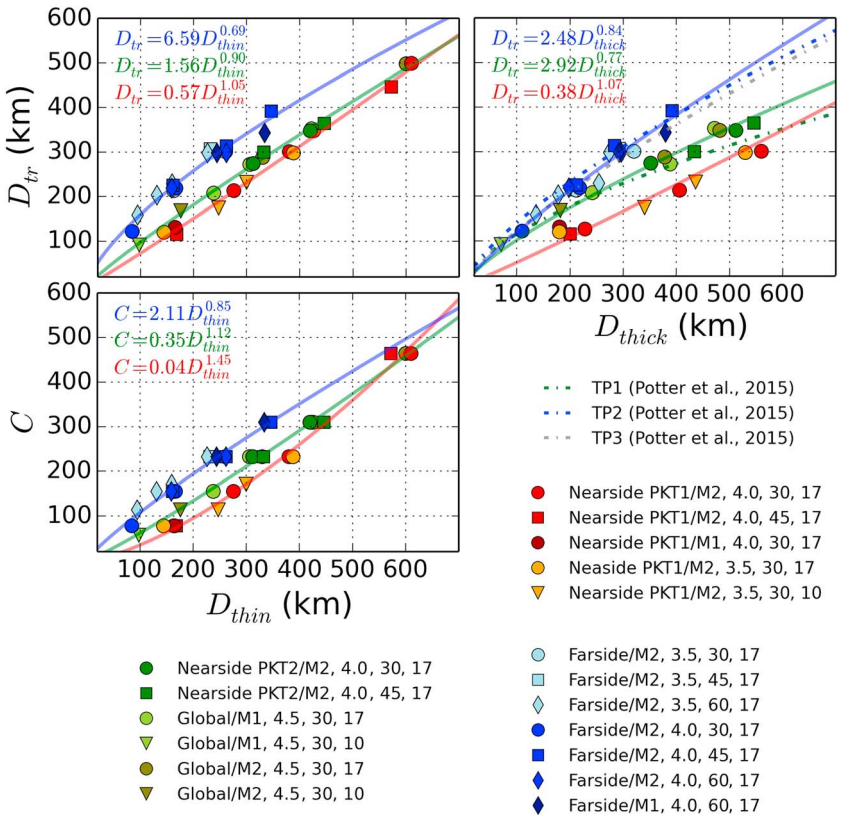

Figure 4. Results from iSALE-2D simulations showing the relationship between (top left) the transient crater size D_{tr} and the final crustal thinning diameter D_{thin}, (bottom left) the impact coupling parameter C and the crustal thinning diameter D_{thin}, and (top right) transient crater size D_{tr} and the crustal thickening diameter D_{thick}. Impact simulations were made by using nine different target temperature profiles, in combination with two assumed impact speeds (10 and 17 km^{-1}) and three preimpact crustal thicknesses (30, 45, and 60 km). Impacts into similar temperature profiles followed a similar trend, and power law fits were made for groups of impacts into a hot target (composed of impacts into targets with temperature profiles denoted as Nearside PKT1/M1 and Nearside PKT1/M2, at 4.0 and 3.5 Ga), an intermediate target (denoted as Global/M1 and Global/M2 at 4.5 Ga and PKT2/M2 at 4.0 Ga), and a cold target (denoted as Farside/M1 and Farside/M2 at 4.0 and 3.5 Ga), shown by the red, green, and blue trend lines, respectively. The coupling parameter C is defined as $Lv^{0.58}$, where L and v are impactor diameter in kilometer and speed in km/s, respectively. The dashed lines correspond to the power law fits reported in *Potter et al.* [2015] for lunar impact basins modeled using comparable temperature profiles.

"intermediate" targets; and all farside profiles were grouped under "cold" targets. The transient crater diameter D_{tr} is smaller than D_{thin} for impacts onto the hot and intermediate targets, while D_{tr} is typically greater than D_{thin} for impacts onto the cold target, irrespective of the preimpact crustal thickness. The power law fits for the results of the three different temperature-related groups are shown in Figure 4 and summarized in Table 1.

Table 1. Summary of the Impact-Scaling Relationships for Impact Basins in Lunar Setting, Separated Between the Cold Target Analogue Typical for the Lunar Farside Hemisphere, Intermediate Target Analogue Typical for the Nearside Hemisphere, Including the Orientale Basin, but Excluding PKT, and the Hot Target Analogue Typical for PKT

	Cold Target (Farside Analogue)	Intermediate Target (Nearside Analogue, Except PKT)	Hot Target (PKT Analogue)
$D_{tr}=A_1D_{thin}^{b1}$	$A_1=6.59$, $b_1=0.69$	$A_1=1.56$, $b_1=0.90$	$A_1=0.57$, $b_1=1.05$
$C=A_2D_{thin}^{b2}$	$A_2=2.11$, $b_2=0.85$	$A_2=0.35$, $b_2=1.12$	$A_2=0.04$, $b_2=1.45$
$D_{tr}=A_3D_{thick}^{b3}$	$A_3=2.48$, $b_3=0.84$	$A_3=2.92$, $b_3=0.77$	$A_3=0.38$, $b_3=1.07$

Another approach for estimating impactor properties directly from observable measures of crater size is by using the so-called "coupling parameter." The coupling parameter C is defined mathematically as the single point-source measure of the coupling of the energy and momentum of the impactor into the planetary surface that determines far-field and late-time behavior [*Holsapple and Schmidt*, 1987]. Assuming that the impactor and target densities are the same, it is defined as the product of the impactor diameter L and impactor velocity υ in the form of $L\upsilon^{\mu}$. The value of the exponent μ was determined experimentally to be in the range of 0.55 to 0.60 [*Holsapple and Schmidt*, 1987], and in this study μ was fixed to the mean value of 0.58. We tested the sensitivity of the relation between C and D_{thin} for different values of the exponent μ from 0.55 to 0.60, finding that the quality of the fit was not significantly affected by the choice of μ (in this range). We also note that for the same D_{thin} value, the uncertainty in C that may come from variations in μ value is not greater than 10%. We prefer to use the impact coupling parameter over the transient crater diameter as a baseline for the impact size, because the transient crater is ambiguous to define in numerical models and is not directly related to any observable crater feature. Moreover, the coupling parameter is directly related to impactor properties.

Our scaling relationships build on the same principle for different, regional, target properties typical for the Moon at the time the basins formed. We derived a relationship between the coupling parameter C and the final basin morphology D_{thin} from our iSALE-2D simulations, similar to the relationship derived between D_{tr} and D_{thin}. Figure 4 (bottom) shows a power law fit for impacts into targets grouped under hot, intermediate, and cold. The power law fit parameters are shown in the figure and summarized in Table 1.

The crust surrounding the mantle uplift is typically thicker than the preimpact crust [*Potter et al*., 2012a]. Crustal thickening occurs because ejection, overturn, and deposition of excavated materials increase the volume of crust at and just exterior to the transient crater rim. This thickened crust collapses inward into the transient crater and abuts the central mantle uplift during the crater rebound phase, producing a collar of thickened crust around the central uplift that *Potter et al*. [2012a] defined as the "thickened crustal annulus." In order to compare our modeling results with similar work by *Potter et al*. [2015], we also considered the scaling relationship between the diameter of the crustal thickening and the transient crater diameter. Figure 4 (top right) shows the relationship between D_{tr} and D_{thick}, as calculated from our iSALE numerical impact simulations grouped under hot, intermediate, and cold targets, as shown similarly in the other two panels. The power law dependences are shown in Figure 4 and Table 1.

The blue and gray dashed lines in Figure 4 correspond to the power law fits for the cold (TP2 and TP3) temperature profiles used by *Potter et al*. [2015]. Their TP2 temperature profile is nearly the same as the Farside/M1 profile at 4.0 Ga used in this work, and their TP3 temperature profile, which is cooler than TP2, is most similar to our Farside/M2 profile at 3.5 Ga. Our results for impacts into cold targets are in agreement with their results using the TP2 and TP3 temperature profiles. The green dashed line shows the power law fit presented by *Potter et al*. [2015] for their TP1 temperature profile, which plots close to our results for the intermediate target. Their TP1 temperature profile is the most similar to our Nearside PKT2/M1 profile at 4.0 Ga. However, their TP1 profile has an initial temperature gradient of 10 K/km in the crust, which is less steep than the initial gradient of ~20 K/km of our intermediate and hot targets. Regardless of the differences in initial temperature gradients, our intermediate target results are in moderate agreement with the results of *Potter et al*. [2015] for their TP1 temperature profile. Our hot temperature profile is hotter than any temperature profile used in *Potter et al*. [2012a, 2015]. It also starts with an initial temperature gradient of ~20 K/km and reaches temperatures much above solidus in the lower crust and upper mantle. Therefore, substantially different results to those presented by *Potter et al*. [2015] are to be expected.

4. Analysis of the GRAIL-Observed Lunar Basins

Analysis of a large data set of GRAIL-observed lunar craters suggested that the onset rim-to-rim crater diameter where the underlying mantle becomes significantly involved in the basin formation process is 218 ± 17 km for craters located in the lunar highlands [*Soderblom et al*., 2015]. Numerical impact modeling of lunar complex craters produced in different target porosities agrees with this onset diameter [*Milbury et al*., 2015]. Therefore, we analyzed the GRAIL-derived crustal thickness models [*Wieczorek et al*., 2013] for all lunar impact basins that are larger than 200 km in rim-to-rim diameter that possess crustal signatures

Table 2. Parameters for GRAIL-Observed Lunar Basins (Larger Than 200 km in Rim Diameter), Arranged From the Largest to the Smallest in Diameter of the Crustal Thinning, for the Four Regions on the Moon: PKT, Nearside Except PKT, Farside Highlands, and the South Pole-Aitken Basin[a]

Name	D_{thin} (km)	h_{thin} (km)	$h \pm \Delta h$ (km)	I (D_{thin})	D_{thick} (km)	h_{thick} (km)	D_{tr} (km)	C
Location: Nearside Hemisphere, Within PKT Only (45°-Spherical Cap Distribution of KREEP Centered Over PKT)								
Imbrium	874	10	28 ± 7	3	971	29	721	769
Serenitatis	600	7	26 ± 8	3	850	32	471	427
Lamont	350	12	28 ± 5	2	700	32	267	195
Serenitatis North	290	13	24 ± 4	3	330	25	219	149
Aestuum	240	12	28 ± 6	3	300	33	180	113
Medii	190	20	35 ± 5	5	530	36	141	81
Vaporum	180	22	29 ± 4	4	540	35	133	75
Copernicus-H	130	16	27 ± 4	4	210	31	95	46
Location: The Remaining Nearside Hemisphere Outside Assumed Region of KREEP Influence (Incl. Orientale Basin)								
Fecunditatis	610	12	29 ± 4	2	860	33	501	461
Crisium	460	2	28 ± 8	2	700	36	389	336
Smythii	440	6	30 ± 8	4	530	35	373	320
Nectaris	410	6	29 ± 7	4	500	37	350	295
Orientale	380	7	36 ± 9	5	530	49	327	271
Humorum	380	8	30 ± 2	4	470	39	327	271
Crisium East	350	9	26 ± 6	2	n/a	n/a	304	247
Asperitatis	350	14	29 ± 5	4	420	33	304	247
Humboldtianum	330	4	28 ± 8	3	380	33	288	232
Cruger-Sirsalis	260	16	32 ± 6	4	370	42	233	177
Mutus-Vlaq	260[b]	21	31 ± 3	7	n/a	n/a	233	177
Schiller-Zucchius	220	10	33 ± 6	3	260	36	200	147
Humboldt	210	21	28 ± 3	2	n/a	n/a	192	140
Grimaldi	190	8	31 ± 7	5	290	43	175	125
Balmer-Kapteyn	130	16	30 ± 4	4	200	33	125	82
Deslandres	110	21	30 ± 3	4	220	34	107	68
Bailly	100	28	36 ± 3	6	210	40	98	61
Schickard	80	31	36 ± 2	5	200	40	81	47
Location: Farside Hemisphere, Highlands Region								
Coulomb-Sarton	300	18	39 ± 6	4	410	47	337	269
Freundlich-Sharanov	290	12	42 ± 9	4	400	49	330	261
Moscoviense North	290	6	37 ± 9	4	410	49	330	261
Moscoviense	260	1	36 ± 11	3	470	45	306	238
Mendel-Rydberg	260	11	35 ± 8	5	410	51	306	238
Fitzgerald-Jackson	250	28	46 ± 5	5	410	51	297	230
TOPO-22	220	23	41 ± 5	4	350	46	272	207
Hertzsprung	220	19	48 ± 7	6	370	58	356	207
Orientale Southwest	180	27	43 ± 5	3	500	48	237	174
Bartels-Voskresenskiy	170	17	35 ± 4	3	210	33	228	166
Schwarzschild	170	27	31 ± 1	3	230	33	228	166
Dirichlet-Jackson	170	38	52 ± 5	5	310	60	228	166
Pasteur	170	33	39 ± 3	2	250	42	228	166
Harkhebi	160	22	31 ± 2	4	250	33	219	158
Korolev	160	36	51 ± 5	5	310	59	219	158
Fowler-Charlier	160	33	46 ± 3	4	270	49	219	158
Mendeleev	150	24	40 ± 4	4	280	45	209	149
Szilard North	150	14	30 ± 6	2	240	35	209	149
Wegener-Winlock	140	33	39 ± 2	3	n/a	n/a	199	141
Lorentz	140	16	35 ± 5	5	230	40	199	141
Fermi	140	31	39 ± 2	3	230	43	199	141
Campbell	120	34	41 ± 2	4	230	44	179	123
Poczobutt	120	29	36 ± 2	4	230	39	179	123
Birkhoff	120	31	41 ± 3	5	210	46	179	123
Milne	120	18	34 ± 4	4	190	39	179	123
d'Alembert	100	35	44 ± 2	4	240	45	158	106
Landau	90	35	42 ± 2	5	210	46	147	97
Sikorsky-Rittenhaus	90	29	33 ± 3	6	200	39	147	97
Gagarin	80	36	40 ± 3	6	n/a	n/a	136	87
Galois	50	40	52 ± 2	5	n/a	n/a	98	59

Table 2. (continued)

Name	D_{thin} (km)	h_{thin} (km)	$h \pm \Delta h$ (km)	l (D_{thin})	D_{thick} (km)	h_{thick} (km)	D_{tr} (km)	C
Location: Farside Hemisphere, the South Pole-Aitken Basin								
Apollo	240[b]	4	29 ± 9	8	320	25	315	222
Poincaré	200[b]	4	19 ± 5	6	240	17	255	191
Amundsen-Ganswindt	180	9	28 ± 5	4	240	34	237	174
Oppenheimer	180	13	20 ± 2	2	230	20	237	174
Ingenii	170	12	27 ± 4	4	n/a	n/a	228	166
von-Kàrmàn M	120	5	17 ± 3	4	250	18	179	123
Schrodinger	160	8	27 ± 5	4	n/a	n/a	219	158
Planck	140	13	28 ± 4	4	190	33	199	141
Leibnitz	140	13	20 ± 2	3	228	21	199	141
TOPO-13	60	26	32 ± 3	7	170	38	62	34

[a]The parameters include the crustal thinning diameter (D_{thin}), the crustal thickness of the crustal cap within the region of the crustal thinning (h_{thin}), preimpact crustal thickness (h), and its standard deviation error in averaging (Δh) and its averaging distance (l), and the crustal thickness at the region of the crustal thickening (D_{thick}). D_{tr} is the diameter of the transient crater, at the moment of the maximum excavation volume. C is the coupling parameter, when projectile diameter is assumed in kilometer and impact speed in km/s. Both D_{tr} and C for lunar impact basins were calculated by using corresponding relationships shown in Table 1.
[b]Determined by hand.

considered to be typical for an impact origin. The total number of investigated impact basins, as numerated by *Neumann et al*. [2015], is 74 (Table 2 and Figure 5).

Azimuthally averaged crustal thickness profiles were generated by using crustal thickness maps derived from the GRAIL gravity and LOLA altimetry data (Figures S1–S4 in the supporting information). Using the same methodology as described in *Wieczorek et al*. [2013], we derived updated models by using the GRGM900C extended mission gravity model. Of the four models presented in *Wieczorek et al*. [2013], we employed model 1 that has a 34 km average crustal thickness, 12% porosity in the crust, a mantle density of 3220 kg m^{-3}, and a downward continuation filter set to 0.5 at degree 80. The profiles were generated for all basins in the database of *Neumann et al*. [2015]. Given that this study is concerned primarily with the region of crustal thinning, and only secondarily with the final basin rim crest, we re-calculated the coordinates of the basin center by using the center of the crustal thinning anomaly. The optimal basin center was achieved by maximizing the variance in the averaged crustal thickness profile by using a conjugate gradient technique. The basin coordinates obtained in this way only varied by about 1° from those given by *Neumann et al*. [2015], and in cases where our technique performed poorly (such as when two basins were partially superposed), we used the coordinates provided by Neumann *et al*.

The size measurements of the lunar impact basins are shown in Table 2, separated according to their location. The measured parameters (as labeled in Figure 2) are the diameter of the crustal thinning (D_{thin}), the crustal thickness at the basin center (h_{thin}), the diameter of the crustal thickening (D_{thick}), the crustal thickness at the diameter of crustal thickening (h_{thick}), and the preimpact crustal thickness (h) averaged over a radial distance (l) of at least 2 D_{thin}. For most basins, the uncertainty for the ambient crustal thickness (Δh) was calculated as the standard deviation from the averaging of the ambient crustal thickness over the averaging distance l. Higher Δh indicated that a basin formed on a larger regional crustal thickness slope. In most cases, the measurements shown in Table 2 were obtained easily in an automatic manner from the crustal thickness profiles. D_{thin} was measured as twice the distance from the basin center to the point where the crustal thickness is equal to the preimpact crustal thickness. D_{thick} was measured from the basin center to the thickest portion of the crust surrounding the mantle uplift. Uncertainties in the radial location of D_{thin} and D_{thick} were set to 10 km, because the radial averaging was made in steps of 5 km. However, due to regional variation in the crustal thickness over which the preimpact crustal thickness was averaged, we rounded the error up to a conservative 10%. We do not provide crustal measurements for basins with anomalous azimuthally averaged crustal profiles because of high uncertainties associated with the measurements. Those basins (from the *Neumann et al*. [2015] database) are Australe North, Bel'kovich, Nubium, Iridum, Keeler West, and Clavius. Similarly, D_{thick} was not measured because of insufficient certainty for the Crisium East, Humboldt, Wegener-Winlock, Gagarin, Galois, Ingenii, and Schrodinger basins. For basins located on a regional slope (Apollo, Poincaré, and Mutus-Vlaq), the D_{thin} was measured by hand. Even though these basins show prominent mantle uplifts, they are located on a regional crustal slope, so our automated algorithm could not be

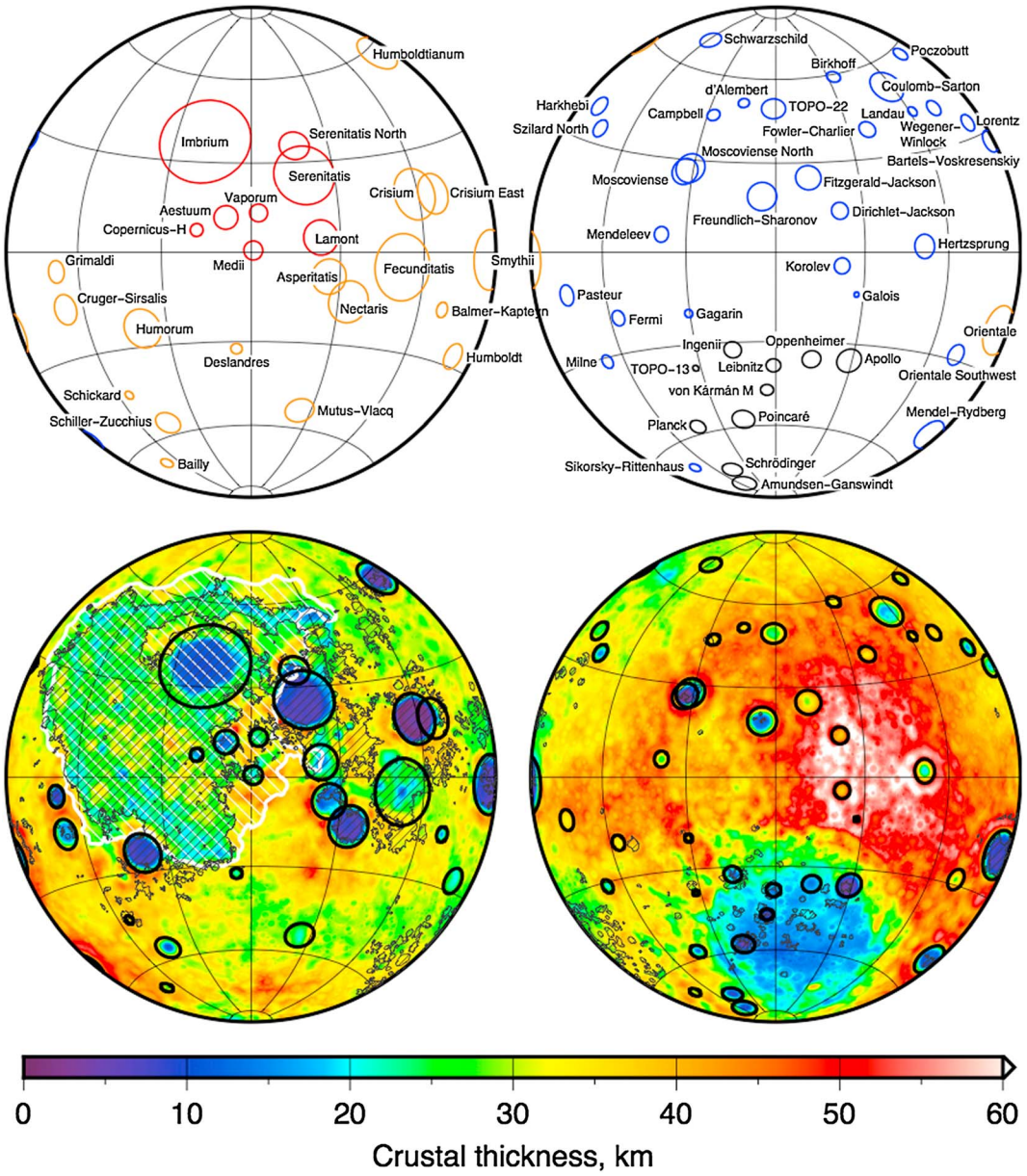

Figure 5. Lunar crustal thickness map (bottom) showing the crustal thinning diameters D_{thin} for all investigated GRAIL-observed basins, with names labeled in the top plot. Basins located within the PKT are marked in red, the remaining nearside basins are marked in orange, basins located in the farside highlands are marked in blue, and basins located within the SP-A are marked in black.

applied. Lunar impact-basin coordinates, basin topographic ring diameters, and Bouguer anomaly diameters and contrasts as obtained by the GRAIL orbiters and reported in *Neumann et al.* [2015] complement the data shown in Table 2.

4.1. Application of Scaling Relationships to GRAIL-Observed Basins

GRAIL-observed lunar basins were grouped into four groups based on their geographic location (Figure 5): nearside basins located within the PKT region (their averaged crustal profiles are shown in Figure S1); nearside basins except in the PKT region, including the Orientale basin located on the limb (Figure S2); farside basins located in the highlands region (Figure S3); and basins located within the SP-A basin (Figure S4). Basins were considered to be located within the PKT region if their centers were closer than 45° away from the geometric center of the Procellarum KREEP Terrane (20°N, 335°E). A similar value of 40° radius was used

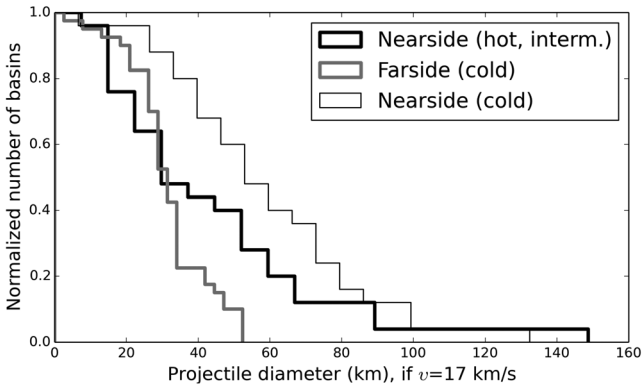

Figure 6. Normalized cumulative size distribution of basin-forming projectiles, assuming a vertical impact speed of 17 km/s. This data set includes all 74 GRAIL-observed impact-basins with clear crustal signatures (Table 2 and Figure 5) and excludes the SP-A basin. All analyzed nearside basins are shown in black, and all farside basins are shown in grey. The thin black line shows projectile diameter estimates when no temperature elevation in the PKT region was considered, and the thick black line when it was considered by applying hot and intermediate temperature scaling relationships.

for the distribution of KREEP-rich materials in the crust as the initial condition in the thermal evolution models of *Laneuville et al*. [2013], also applied in this study.

We applied the upgraded scaling relationships (D_{tr}-D_{thin} and the C-D_{thin}) to the GRAIL-observed lunar basins in order to estimate their transient crater diameters D_{tr} and coupling parameter C in each case (Table 2). In cases where D_{thin} could not be measured but D_{thick} could, we applied our D_{tr}-D_{thick} relationship to estimate the transient crater diameter. We assumed that each of the four geographic groupings of basins corresponded to one of our three groupings of temperature profiles (cold, intermediate, and hot) when they formed. Basins located within the PKT were assumed to have formed with a hot crustal temperature profile, the other nearside basins (including the Orientale basin located on the limb) were assumed to have formed in a crust with an intermediate temperature profile, and all farside basins (both in the highlands region and the SP-A basin) were assumed to have formed in a crust with a cold temperature profile.

We excluded the SP-A basin from our detailed analysis because it is both the oldest impact basin on the Moon and also likely the largest. Its size implies that the curvature of the Moon likely played a role in its formation [*Andrews-Hanna and Zuber*, 2010], and its age implies that the crustal and mantle temperatures were possibly more extreme than the ones described for the later basin-forming epoch. Therefore, the SP-A basin is unlikely to satisfy the impact scaling relationships developed in this work. The formation of the SP-A was previously investigated in detail in *Potter et al*. [2012b].

The coupling parameter C is a product of the impactor mass and speed, and the simplest deconvolution of this product would be to assume one (average) impact velocity (and an average impact angle). Assuming a projectile density the same as that of the mantle and the same impact speed of about 17 km/s, Figure 6 shows a cumulative size distribution of projectiles that could have formed GRAIL-observed basins analyzed in this work. The thick black and grey lines show the normalized projectile size distributions for basins located on the nearside and the farside hemisphere, respectively. In this case, the model predicts that the basin-forming impactors to ranged between 10 km and 150 km. This impactor range is in agreement with the projectile size estimates reported by *Potter et al*. [2015] for the basin-forming epoch. We note that only basins with clear crustal signatures were included in projectile size distributions.

The thin black line in Figure 6 shows the cumulative projectile size distribution for all considered GRAIL-observed basins on the nearside hemisphere when the temperature elevation is not taken into consideration. It demonstrates the importance of the target temperature, because the two black lines are distinctively different. Also, once the temperature effects were accounted for, by applying the appropriate scaling relationships (Table 1), the projectile size distributions between the nearside and the farside hemispheres are more comparable. Therefore, in further studies of the early lunar (and generally, the solar system) bombardment, one must consider the target properties, namely, the temperature.

4.2. GRAIL-Observed Subsurface Morphology of Impact Basins

As previously discussed in *Miljković et al*. [2013] and *Neumann et al*. [2015], the largest nearside basins (Figure 5, also Figures S1 and S2) are consistently larger than the largest basins on the farside (Figures S3 and S4), which is likely a consequence of the nearside crust and upper mantle being warmer than that of

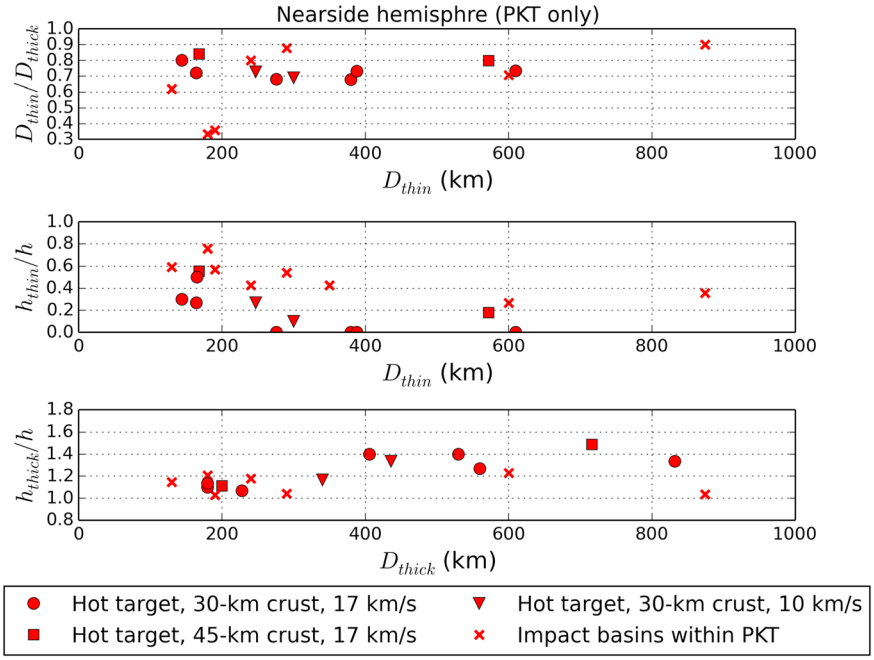

Figure 7. (top) The ratio of the crustal thinning and the crustal thickening diameters as a function of the crustal thinning diameter. (middle) The ratio of the thinnest crust in the central region of a basin (thickness of the crustal cap) and the preimpact crustal thickness. (bottom) The ratio of the crustal thickness at the crustal thickening diameter (the thickest crust within a basin) and the preimpact crustal thickness. The crosses mark the GRAIL-observed lunar basins within the PKT region. The observations are compared against the numerical modeling results (shown by filled symbols) for impacts into hot target properties comparable to the lunar PKT region at the time the majority of lunar basins formed.

the farside at the time these basins formed [e.g., *Wieczorek and Phillips*, 2000; *Jolliff et al.*, 2000; *Korotev*, 2000; *Zhong et al.*, 2000; *Hess and Permentier*, 2001; *Laneuville et al.*, 2013]. Also, basins like the Crisium basin (Figure S2) and the Moscoviense basin (Figure S3) have crustal thicknesses approaching zero beneath their central mare deposits, which suggests that the underlying mantle might have been excavated and exposed on the surface during the basins forming process [*Miljković et al.*, 2015]. Further analyses of the crustal thickness profiles included analyses of the subsurface basin structure by investigating the extent of mantle uplift, crustal thinning, and crustal thickening within a basin (Figures 7–9).

Figures 7–9 show the measures and comparisons of three different morphological features for lunar basins located within the PKT, the nearside hemisphere except PKT, and the farside (both the highland region and the SP-A), respectively. Figures 7–9 (top) show the size of the crustal thinning region compared to the crustal thickening region, as a ratio of the two diameters (D_{thin}/D_{thick}), as a function of the crustal thinning diameter for the GRAIL-observed basins (open symbols). Superimposed are our numerical modeling results typical for the respective regions on the Moon at the time lunar basins formed (closed symbols). Similarly, Figures 7–9 (middle) show the ratio of the crustal thickness in the basin center and the preimpact crustal thickness (h_{thin}/h) for the GRAIL-observed basins and our numerical modeling results, and Figures 7–9 (bottom) show the ratio of the crustal thickness at the crustal thickening diameter (the thickest crust within a basin) and the preimpact crustal thickness (h_{thick}/h) for GRAIL-observed basins and our numerical modeling results, all as a function of basin size presented via D_{thin}.

For our iSALE-2D simulations, Figures 7–9 (top) show that there is no resolvable difference in the D_{thin}/D_{thick} ratio between impacts onto crust that is 30, 45, and 60 km thick, when using similar temperature profiles. However, our numerical modeling results for basin-forming impacts onto a hot target (Figure 7) show a slightly smaller D_{thin}/D_{thick} ratio than for basins that formed in a cooler target (Figure 9), for $D_{thin} >$ ~200 km. This is likely a result of the hotter crust being weaker, which allows for the inflow of more crustal material into the basin during the collapse stage of the basin forming process [*Miljković et al.*, 2013; *Freed et al.*, 2014]. For $D_{thin} <$ ~200 km, our simulation does not reproduce the observed mantle uplift

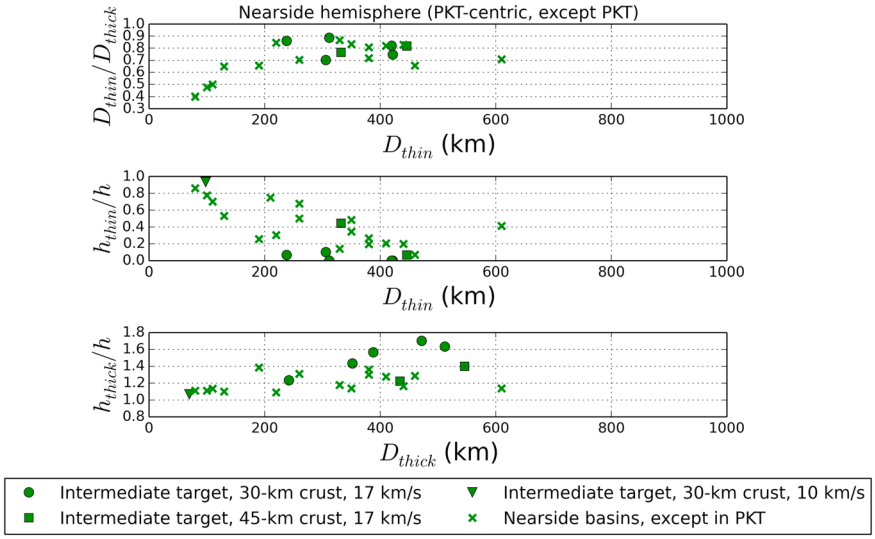

Figure 8. (top) The ratio of the crustal thinning and the crustal thickening diameters as a function of the crustal thinning diameter. (middle) The ratio of the thinnest crust in the central region of a basin (thickness of the crustal cap) and the preimpact crustal thickness. (bottom) The ratio of the crustal thickness at the crustal thickening diameter (the thickest crust within a basin) and the preimpact crustal thickness. The crosses mark the GRAIL-observed lunar basins on the nearside hemisphere, except the PKT region. The observations are compared against the numerical modeling results (shown by filled symbols) for impacts into intermediate target properties comparable to the nearside hemisphere (including Oriental and excluding PKT) at the time the majority of lunar basins formed.

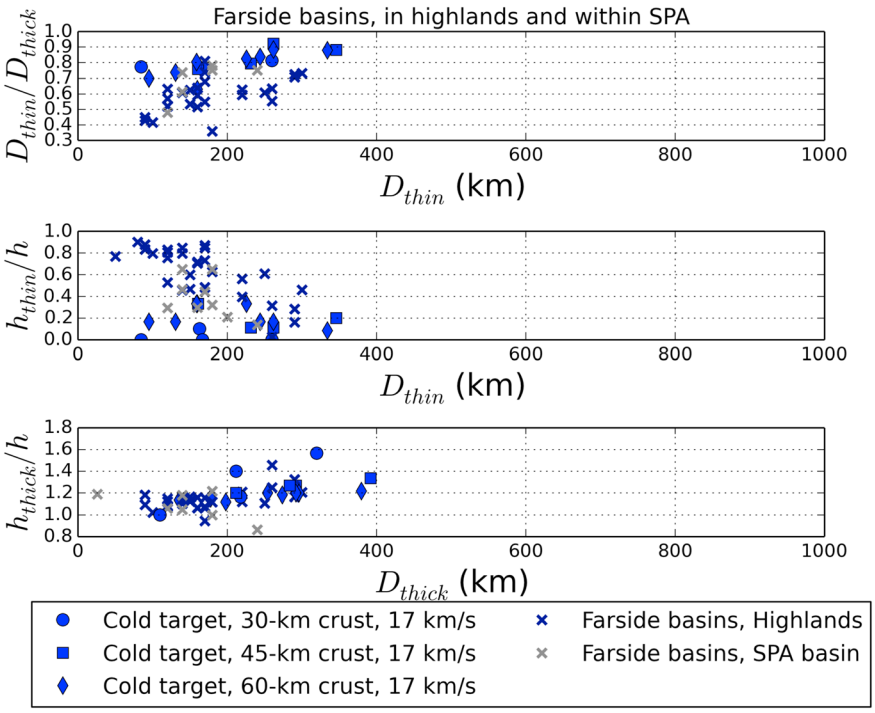

Figure 9. (top) The ratio of the crustal thinning and the crustal thickening diameters as a function of the crustal thinning diameter. (middle) The ratio of the thinnest crust in the central region of a basin (thickness of the crustal cap) and the preimpact crustal thickness. (bottom) The ratio of the crustal thickness at the crustal thickening diameter (the thickest crust within a basin) and the preimpact crustal thickness. The crosses mark the GRAIL-observed lunar basins on the farside hemisphere (both highlands and the SP-A basin). The observations are compared against the numerical modeling results (shown by filled symbols) for impacts into cold target properties comparable to the lunar farside hemisphere at the time the majority of lunar basins formed.

structure in lunar basins. This could be due to the greater mantle uplift than what may be realistic in the case of the cold crust used to model the farside basins (Figure 8). This effect will be investigated in future work.

We also observed that the D_{thin}/D_{thick} ratio of basins in cold targets is, on average, slightly higher in numerically modeled basins than in the GRAIL-observed lunar basins (Figure 8). This could be due to the fact that our models only simulate basin formation for the first 2 h after impact, while the observational data show the present-day basin structure that might have been affected by long-term modification processes, such as viscous relaxation [e.g., *Wieczorek and Phillips*, 2000; *Mohit and Phillips*, 2006; *Kamata et al*., 2013; *Melosh et al*., 2013; *Freed et al*., 2014].

Our numerical simulations showed that the collapse of the transient crater was considerably more important in the hot and large basins than in the cooler targets and/or smaller basins. This collapse process could have resulted in a near-complete removal of the crustal thickening region, particularly for the largest basins. Consistent with observations, Figures 7–9 show that the h_{thick}/h ratio is lower for the hot target simulations than the cold ones. For crustal thickening diameters larger than about 200 km, our numerical results showed that the h_{thick}/h ratio depends somewhat on the preimpact crustal thickness, although this effect is secondary to the larger temperature effects.

Numerical modeling showed that smaller or slower impactors excavate and displace less crustal material, which subsequently gives rise to less mantle uplift during the collapse of the transient crater. Therefore, the crustal coverage of the mantle uplift is thicker in less energetic impacts. However, in larger impacts, particularly in a hot target, the crust flows back onto the melt pool, producing different outcome in basin formation (as explored in detail in *Freed et al*. [2014], and as defined as the crustal cap). Our numerical modeling also suggested that the formation of larger lunar impact basins in a hot crust results in a thicker crustal cap covering the mantle uplift than for basins formed in a cooler crust.

Some numerical simulations resulted in the exposure of mantle materials at the surface level (i.e., where h_{thin} is zero). Mantle exposures occurred most commonly for impacts in the thinnest crust (30 km) and for the largest basins that formed in cooler targets. Nevertheless, the GRAIL-obtained averaged crustal thickness profiles for the majority of lunar impact basins imply the existence of a crustal cap (h_{thin} in Table 2) of several kilometers in thickness (including deposits of mare basalts, if present). This discrepancy between simulations and the GRAIL data could potentially be the result of postimpact viscous relaxation [e.g., *Melosh et al*., 2013; *Dombard et al*., 2013; *Freed et al*., 2014], differentiation of an impact melt pool that formed additional crustal materials [e.g., *Vaughan and Head*, 2014; *Hurwitz and Kring*, 2014], or perhaps by an underestimation of the quantity of mare basalts and their intrusive equivalents within the basin [e.g., *Kiefer et al*., 2014; *Gong et al*., 2016].

5. Conclusions

Understanding the effects of target properties on impact basin formation leads to a better customization of impact scaling relationships that are useful for inferring impactor properties from observed basin structure. Their utility was previously demonstrated by an application of the standard scaling laws for simple and complex craters [e.g., *Croft*, 1985; *Melosh*, 1989; *Holsapple*, 1993] and initiated recently for lunar impact basins [*Ivanov et al*., 2010; *Potter et al*., 2012a, 2015].

We introduced the use of the crustal thinning diameter (D_{thin}) as a new preferred measure of basin and impactor size, because it can be readily determined from crustal thickness maps derived from gravity and topography data of sufficiently high spatial resolution. The region of crustal thinning is better preserved than surface morphology and topographic expression, and it can be easily measured in impact simulations. In addition, we showed that it was advantageous to use the impact coupling parameter over the transient crater diameter as a measure for the impact size, because the transient crater is not directly related to any observable crater feature and is ambiguous to define in numerical models. Moreover, the coupling parameter measures impactor quantities directly.

This work emphasized the importance of target temperature and its significant effect on pristine impact basin morphology. We also showed that the ambient crustal thickness had a lesser effect on basin morphology in comparison to the target temperature effect. Our numerical modeling results suggested that the target

temperature affects the final basin size and that it also affects the extent of the crustal thinning, mantle uplift, thickening of the crust surrounding the mantle uplift, and the thickness of the crustal cap that covers up the mantle uplift.

In summary, our numerical modeling showed the following:

1. The crustal thinning diameter is generally larger than the transient crater diameter for impacts into the nearside hemisphere and global early Moon where crustal temperatures were high, while the transient crater diameter is generally larger than the crustal thinning diameter for impacts on the farside hemisphere where the temperatures are cooler. This tendency was found to be independent of the preimpact crustal thickness.
2. There is no significant difference in the ratio of the crustal thinning to crustal thickening diameters between impacts into 30, 45, and 60 km preimpact crustal thickness when using similar temperature profiles. However, simulations of basin-forming impacts into hot targets showed smaller crustal thinning to crustal thickening diameter ratios than basins that formed in cooler targets.
3. For crustal thickening diameters larger than about 200 km, our numerical results showed that the ratio of the thickest crust within a basin and the preimpact crustal thickness depends on the preimpact crustal thickness, although this effect is secondary to the aforementioned temperature effects.
4. The crustal cap in the basin interior is thicker both for less energetic impacts and hotter targets.

We developed basin scaling relationships that account for the different temperature conditions that would be experienced during the Moon's basin-forming epoch (4.5–3.5 Ga ago) and applied them to the GRAIL-observed lunar basins (according to their location and respective assumed target temperature) to estimate their transient crater sizes and possible impact conditions. Predicted impactor sizes range from 10 to 150 km in diameter for craters larger than 200 km (in rim-to-rim diameter) on the Moon, for an average vertical component of the impact speed of 17 km s^{-1}. The estimated projectile size distribution is now more comparable between the nearside and the farside hemisphere. When considering the impact flux in the early solar system (not only the Moon), one should always consider the possible implications of target properties, such as temperature, on the large crater formation process.

Acknowledgments

The GRAIL mission is supported by the Discovery Program of NASA and is performed under contract to the Massachusetts Institute of Technology and the Jet Propulsion Laboratory, California Institute of Technology. Additional support for this work was provided by the French Space Agency (CNES). We gratefully acknowledge the developers of iSALE- 2D, including Kai Wünnemann, Dirk Elbeshausen, Boris Ivanov, and Jay Melosh. G.S.C. was funded by STFC grant ST/N000803/1. The data used in this study are attached as supporting information and are also available upon request from the main author (Katarina. Miljkovic@curtin.edu.au).

References

Amsden, A. A., H. M. Ruppel, and C. W. Hirt (1980), SALE: A simplified ALE computer program for fluid flow at all speeds, *Report LA-8095*, Los Alamos National Laboratories, N. Mex., 105 pp.

Andrews-Hanna, J. C., and M. T. Zuber (2010), Elliptical craters and basins on the terrestrial planets, in *Large Meteorite Impacts and Planetary Evolution IV*, edited by Gibson, R. L., Reimold, W. U., *Geol. Soc. Am. Spec. Pap*. 465, 1–13, doi:10.1130/2010.2465(01).

Baker, D. M. H., J. W. Head, C. I. Fasset, S. J. Kadish, D. A. Smith, M. T. Zuber, and G. A. Neumann (2011), The transition from complex crater to peak-ring basin on the Moon: New observations from the Lunar Orbiter Laser Altimeter (LOLA) instrument, *Icarus*, *214*, 377–393, doi:10.1016/j.icarus.2011.05.030.

Benz, W., A. G. W. Cameron, and H. J. Melosh (1989), The origin of the Moon and the single-impact hypothesis III. *Icarus*, *81*, 113–131.

Besserer, J., F. Nimmo, M. A. Wieczorek, R. C. Weber, W. S. Kiefer, P. J. McGovern, J. C. Andrews-Hanna, D. E. Smith, and M. T. Zuber (2014), GRAIL gravity constraints on the vertical and lateral density structure of the lunar crust, *Geophys. Res. Lett.*, *41*, 5771–5777, doi:10.1002/2014GL060240.

Bottke, W. F., D. Vokrouhlicky, D. Minton, D. Nesvorny, A. Morbidelli, R. Brasser, B. Simonson, and H. F. Levison (2012), An archaean heavy bombardment from a destabilized extension of the asteroid belt, *Nature*, *485*(485), 78–81, doi:10.1038/nature10967.

Bratt, S. T., S. C. Solomon, J. W. Head, and C. H. Thurber (1985), The deep structure of lunar basins: Implications for basin formation and modification, *J. Geophys. Res.*, *90*(B4), 3049–3064, doi:10.1029/JB090iB04p03049.

Collins, G. S., H. J. Melosh, and B. A. Ivanov (2004), Damage and deformation in numerical impact simulations, *Meteorit. Planet. Sci.*, *39*(2), 217–231, doi:10.1111/j.1945-5100.2004.tb00337.x.

Croft, S. K. (1985), The scaling of complex craters, *J. Geophys. Res.*, *90*, C828–C842, doi:10.1029/JB090iS02p0C828.

Dombard, A. J., S. A. Hauck II, and J. A. Balcerski (2013), On the origin of mascon basins on the Moon (and beyond), *Geophys. Res. Lett.*, *40*, 28–32, doi:10.1029/2012GL054310.

Elbeshausen, D., K. Wünneman, and G. S. Collins (2009), Scaling of oblique impacts in frictional targets: Implications for crater size and formation mechanisms, *Icarus*, *204*, 716–731, doi:10.1016/j.icarus.2009.07.018.

Fassett, C. I., J. W. Head, S. J. Kadish, E. Mazarico, G. A. Neumann, D. E. Smith, and M. T. Zuber (2012), Lunar impact basins: Stratigraphy, sequence and ages from superposed impact crater populations measured from Lunar Orbiter Laser Altimeter (LOLA) data, *J. Geophys. Res.*, *117*, E00H06, doi:10.1029/2011JE003951.

Freed, A. M., B. C. Johnson, D. M. Blair, H. J. Melosh, G. A. Neumann, R. J. Philips, S. C. Solomon, M. A. Wieczorek, and M. T. Zuber (2014), The formation of lunar mascons from impact to contemporary form, *J. Geophys. Res. Planets*, *119*, 2378–2397, doi:10.1002/2014JE004657.

Gomes, R., H. F. Levison, K. Tsiganis, and A. Morbidelli (2005), Origin of the cataclysmic Late Heavy Bombardment period of the terrestrial planets, *Nature*, *435*, 466–469, doi:10.1038/nature03676.

Gong, S., M. A. Wieczorek, F. Nimmo, W. S. Kiefer, J. W. Head, C. Huang, D. E. Smith, and M. T. Zuber (2016), Thicknesses of mare basalts on the Moon from gravity and topography, *J. Geophys. Res. Planets*, *121*, 854–870, doi:10.1002/2016JE005008.

Hartmann, W. K., and G. P. Kuiper (1962), Concentric structures surrounding lunar basins, *Comm. Lunar and Planetary Lab.*, Univ. Arisona, 1, 51–66.

Hess, P. C., and E. M. Permentier (2001), Thermal evolution of a thicker KREEP liquid layer, *J. Geophys. Res.*, *106*, 28,023–28,032, doi:10.1029/2000JE001416.
Holsapple, K. A. (1993), The scaling of impact process in planetary sciences, *Annu. Rev. Earth Planet. Sci.*, *21*, 333–373, doi:10.1146/annurev.ea.21.050193.002001.
Holsapple, K. A., and R. M. Schmidt (1987), Point source solutions and coupling parameters in cratering mechanics, *J. Geophys. Res.*, *92*(B7), 6350–6376, doi:10.1029/JB092iB07p06350.
Hurwitz, D. M., and D. A. Kring (2014), Differentiation of the South Pole–Aitken basin impact melt sheet: Implications for lunar exploration, *J. Geophys. Res. Planets*, *119*, 1110–1133, doi:10.1002/2013JE004530.
Ivanov, B. A., H. J. Melosh, and E. Pierazzo (2010), Basin-forming impacts: Reconnaissance modeling, in *Large Meteorite Impacts and Planetary Evolution IV*, edited by R. L. Gibson and W. U. Reimold, *Geol. Soc. Am. Spec. Pap.*, 465, 29–49, doi:10.1130/2010.2465(03).
Johnson, B. C., and H. J. Melosh (2012), Impact spherules as a record of an ancient heavy bombardment of Earth, *Nature*, *485*, 75–77, doi:10.1038/nature10982.
Johnson, B. C., J. C. Andrews-Hanna, G. S. Collins, H. J. Melosh, J. W. Head, D. M. Blair, A. M. Freed, K. Miljković, J. M. Soderblom, and M. T. Zuber (2015), The formation of lunar multi-ring basins, *Lunar Planet. Sci.*, LPI Contribution, No. 1362.
Jolliff, B. L., J. J. Gillis, L. A. Haskin, R. L. Korotev, and M. A. Wieczorek (2000), Major lunar crustal terranes: Surface expressions and crust-mantle origins, *J. Geophys. Res.*, *105*, 4197–4216, doi:10.1029/1999JE001103.
Kamata, S., et al. (2013), Viscoelastic deformation of lunar impact basins: Implications for heterogeneity in the deep crustal paleo-thermal state and radioactive element concentration, *J. Geophys. Res. Planets*, *118*, 398–415, doi:10.1002/jgre.20056.
Kiefer, W. S., et al. (2014), The contribution of impact melt sheets to lunar impact basin gravity anomalies, 45th *Lunar Planet. Sci. Conference*, LPI Contribution No. 2831.
Korotev, R. L. (2000), The great lunar hot spot and the composition and origin of the Apollo mafic ("LKFM") impact-melt breccias, *J. Geophys. Res.*, *105*, 4317–4346, doi:10.1029/1999JE001063.
Kring, D. A., and B. A. Cohen (2002), Cataclysmic bombardment throughout the inner solar system 3.9–4.0 Ga, *J. Geophys. Res.*, *107*(E2), 5009, doi:10.1029/2001JE001529.
Laneuville, M., M. A. Wieczorek, D. Breuer, and N. Tosi (2013), Asymmetric thermal evolution of the Moon, *J. Geophys. Res. Planets*, *118*, 1435–1452, doi:10.1002/jgre.20103.
Le Feuvre, M., and M. A. Wieczorek (2011), Nonuniform cratering of the Moon and a revised crater chronology of the inner Solar System, *Icarus*, *214*, 1–20, doi:10.1016/j.icarus.2011.03.010.
Lemoine, F. G., et al. (2014), GRGM900C: A degree 900 lunar gravity model from GRAIL primary and extended mission data, *Geophys. Res. Lett.*, *41*, 3382–3389, doi:10.1002/2014GL060027.
Melosh, H. J. (1989), *Impact Cratering. A Geological Process*, *Oxford Monographs on Geology and Geophysics*, 245 pp., Oxford Univ. Press, New York, USA.
Melosh, H. J., et al. (2013), The origin of lunar mascon basins, *Science*, *340*, 1552–1555, doi:10.1126/science.1235768.
Milbury, C., B. C. Johnson, H. J. Melosh, G. S. Collins, D. M. Blair, J. M. Soderblom, F. Nimmo, C. J. Bierson, R. J. Phillips, and M. T. Zuber (2015), Preimpact porosity controls the gravity signature of lunar craters, *Geophys. Res. Lett.*, *42*, 9711–9716, doi:10.1002/2015GL066198.
Miljković, K., M. A. Wieczorek, G. S. Collins, M. Laneuville, G. A. Neumann, H. J. Melosh, S. C. Solomon, R. J. Phillips, D. E. Smith, and M. T. Zuber (2013), Asymmetric distribution of lunar impact basins caused by variations in target properties, *Science*, *342*, 724–726, doi:10.1126/science.1243224.
Miljković, K., M. A. Wieczorek, G. S. Collins, S. C. Solomon, D. E. Smith, and M. T. Zuber (2015), Excavation of the mantle in basin-forming impact events on the Moon, *Earth Planet. Sci. Lett.*, *409*, 243–251, doi:10.1016/j.epsl.2014.10.041.
Mohit, P. S., and R. J. Phillips (2006), Viscoelastic evolution of lunar multiring basins, *J. Geophys. Res.*, *111*, E12001, doi:10.1029/2005JE002654.
Müller, P. M., and W. L. Sjogren (1968), Mascons: Lunar mass concentrations, *Science*, *161*, 680–684.
Neumann, G. A., M. T. Zuber, D. E. Smith, and F. G. Lemoine (1996), The lunar crust: Global structure and signature of major basins, *J. Geophys. Res.*, *101*, 16,841–16,863, doi:10.1029/96JE01246.
Neumann, G. A., et al. (2015), Lunar impact basins revealed by Gravity Recovery and Interior Laboratory measurements, *Sci. Adv.*, *1*(9), e1500852, doi:10.1126/sciadv.1500852.
Osinski, G. R., and E. Pierazzo (2012), Impact cratering: Processes and products, in *Impact Cratering Processes and Products*, edited by G. R. Osinski and E. Pierazzo, pp. 1–20, John Wiley, Chichester, U. K., doi:10.1002/9781118447307.ch1.
Phillips, R. J., J. E. Conel, E. A. Abbott, W. L. Sjogren, and J. B. Morton (1972), Mascons: Progress toward a unique solution for mass distribution, *J. Geophys. Res.*, *77*(35), 7106–7114, doi:10.1029/JB077i035p07106.
Pierazzo, E., and H. J. Melosh (2000), Understanding oblique impacts from experiments, observations, and modeling, *Annu. Rev. Earth Planet. Sci.*, *28*, 141–167, doi:10.1146/annurev.earth.28.1.141.
Pierazzo, E., N. A. Artemieva, and B. A. Ivanov (2005), Starting conditions for hydrothermal systems underneath martian craters: Hydrocode modeling, in *Large Meteorite Impacts III, Spec. Pap. vol. 384*, edited by T. Kenkmann, F. Hörz, A. Deutsch, pp. 443–457, Geol. Soc. of Am., Boulder, Colo.
Pierazzo, E., et al. (2008), Validation of numerical codes for impact and explosion cratering: Impacts on strengthless and metal targets, *Meteorit. Planet. Sci.*, *43*, 1917–1938, doi:10.1111/j.1945-5100.2008.tb00653.x.
Potter, R., D. A. Kring, G. S. Collins, W. S. Kiefer, and P. J. McGovern (2012a), Estimating transient crater size using the crustal annular bulge: Insights from numerical modeling of lunar basin-scale impacts, *Geophys. Res. Lett.*, *39*, L18203, doi:10.1029/2012GL052,981.
Potter, R. W. K., G. S. Collins, W. S. Kiefer, P. J. McGovern, and D. A. Kring (2012b), Constraining the size of the South Pole-Aitken basin impact, *Icarus*, *220*, 730–743, doi:10.1016/j.icarus.2012.05.032.
Potter, R. W. K., D. A. Kring, G. S. Collins, W. S. Kiefer, and P. J. McGovern (2013), Numerical modeling of the formation and structure of the Orientale impact basin, *J. Geophys. Res. Planets*, *118*, 963–979, doi:10.1002/jgre.20080.
Potter, R. W. K., D. A. Kring, and G. S. Collins (2015), Scaling of basin-sized impacts and the influence of target temperature, in *Meteorite Impacts and Planetary Evolution V*, edited by G. R. Osinski and D. A. Kring, *Geol. Soc. Am. Spec. Pap.*, 518, 99–113, doi:10.1130/2015.2518(06).
Schmidt, R. M., and K. R. Housen (1987), Some recent advances in the scaling of impact and explosion cratering, *Int. J. Impact Eng.*, *5*, 543–560, doi:10.1016/0734-743X(87)90069-8.
Smith, D. E., et al. (2010), Initial observations from the Lunar Orbiter Laser Altimeter (LOLA). *Geophys. Res. Lett.*, *37*, L18204, doi:10.1029/2010GL043751.
Soderblom, J. M., et al. (2015), Production and saturation of porosity in the lunar highlands from impact cratering, *Geophys. Res. Lett.*, *42*, 6939–6944, doi:10.1002/2015GL065022.

Spudis, P. D. (1993), *The Geology of Multi-ring Impact Basins*, 277 pp., Cambridge Univ. Press, New York, USA.
Stöffler, D., and G. Ryder (2001), Stratigraphy and isotope ages of lunar geologic units: Chronological standard for the inner solar system, in *Chronology and Evolution of Mars*, *Space Sci. Ser. ISSI*, vol. 96, edited by R. Kallenbach, J. Geiss, and W. K. Hartmann, pp. 9–54, Kluwer Acad. Publ., Boston.
Tera, F., D. A. Papanastassiou, and G. J. Wasserburg (1974), Isotopic evidence for a terminal lunar cataclysm, *Earth Planet. Sci. Lett.*, *22*, 1–21, doi:10.1016/0012-821X(74)90059-4.
Vaughan, W. M., and J. W. Head (2014), Impact melt differentiation in the South Pole-Aitken basin: Some observations and speculations, *Planet. Space Sci.*, *91*, 101–116, doi:10.1016/j.pss.2013.11.010.
Wieczorek, M. A., and R. J. Phillips (1999), Lunar multiring basins and the cratering process, *Icarus*, *139*, 246–259, doi:10.1006/icar.1999.6102.
Wieczorek, M. A., and R. J. Phillips (2000), The "Procellarum KREEP Terrane": Implications for mare volcanism and lunar evolution, *J. Geophys. Res.*, *105*, 20,417–20,430, doi:10.1029/1999JE001092.
Wieczorek, M. A., et al. (2013), The crust of the Moon as seen by GRAIL, *Science*, *339*, 671–675, doi:10.1126/science.1231530.
Wilhelms, D. E. (1987), *The Geologic History of the Moon*, *U. S. Geol. Sur. Prof. Pap.*, vol. 1348.
Wise, D. U., and M. T. Yates (1970), Mascons as structural relief on a lunar Moho, *J. Geophys. Res.*, *75*(2), 261–268, doi:10.1029/JB075i002p00261.
Wünnemann, K., G. S. Collins, and H. J. Melosh (2006), A strain-based porosity model for use in hydrocode simulations of impacts and implications for transient crater growth in porous targets, *Icarus*, *180*, 514–527, doi:10.1016/j.icarus.2005.10.013.
Zhong, S., E. M. Parmentier, and M. T. Zuber (2000), A dynamic origin for the global asymmetry of lunar mare basalts, *Earth Planet. Sci. Lett.*, *177*, 131–140, doi:10.1016/S0012-821X(00)00041-8.
Zuber, M. T., D. E. Smith, F. G. Lemoine, and G. A. Neumann (1994), The shape and internal structure of the Moon from the Clementine mission, *Science*, *266*, 1839–1843, doi:10.1126/science.266.5192.1839.
Zuber, M. T., et al. (2013), Gravity field of the Moon from the Gravity Recovery and Interior Laboratory (GRAIL) mission, *Science*, *339*, 668–671, doi:10.1126/science.1231507.